Korean J. Chem. Eng.
DOI: 10.1007/s11814-021-0846-9

pISSN: 0256-1115
eISSN: 1975-7220

Photocatalytic removal of Rhodamine B in water using g-C_3N_4/MIL-53(Fe) material under LED visible light with persulfate activation

Nguyen Trung Dung*,†, Nguyen Van Hiep*, Manh B. Nguyen,***, Vu Dinh Thao*, and Nguyen Nhat Huy****,*****,†**

*Faculty of Physical and Chemical Engineering, Le Quy Don Technical University, 236 Hoang Quoc Viet St., Bac Tu Liem District, Hanoi, Vietnam
**Institute of Chemistry (IOC), Vietnam Academy of Science and Technology (VAST), 18 Hoang Quoc Viet, Cau Giay District, Hanoi, Viet Nam
***Hanoi University of Science and Technology (HUST), 01 Dai Co Viet Road, Hai Ba Trung District, Hanoi, Viet Nam
****Faculty of Environment and Natural Resources, Ho Chi Minh City University of Technology (HCMUT), 268 Ly Thuong Kiet St., District 10, Ho Chi Minh City, Vietnam
*****Vietnam National University Ho Chi Minh City, Linh Trung Ward, Thu Duc City, Ho Chi Minh City, Vietnam
(*Received 17 January 2021 • Revised 22 April 2021 • Accepted 16 May 2021*)

Abstract−Photocatalysis is usually considered as one of the most effective methods for treating non-biodegradable pollutants commonly found in textile wastewater. In this study, the photocatalyst of g-C_3N_4/MIL-53(Fe) was synthesized by the hydrothermal method and applied for the removal of Rhodamine B (RhB) in water. The photocatalytic material was characterized by X-ray diffraction, Fourier-transform infrared spectroscopy, scanning electron microscopy, energy-dispersive X-ray spectroscopy, Brunauer-Emmett-Teller analysis, UV-Vis diffuse reflectance spectroscopy, and X-ray photoelectron spectroscopy. The results showed that the g-C_3N_4 doped MIL-53(Fe) with 97 wt% of MIL-53(Fe) works effectively under visible light and the presence of oxidants ($Na_2S_2O_8$). RhB removal efficiency can be more than 99% with 20 mg/L of RhB, 300 mg/L of catalyst, 200 mg/L of $Na_2S_2O_8$, and pH 3. In addition, the photocatalytic degradation mechanism of RhB with g-C_3N_4/MIL-53(Fe) was also proposed, which could be improved and studied for a wide range of applications in textile wastewater treatment.

Keywords: Rhodamine B, g-C_3N_4, MIL-53(Fe), Photocatalysis, Visible Light

INTRODUCTION

Advanced oxidation process based on sulfate radical ($SO_4^{\bullet-}$) is an emerging technology for persistent organics removal in water due to its strong oxidation potential and high efficiency. The sulfate radical has higher redox potential (2.5-3.1 V) than hydroxyl radical ($HO^{\bullet}$, 2.8 V). It has more selective oxidation for pollutants with aromatic ring and unsaturated bonds with higher reaction rate of 10^6-10^9 $M^{-1}\cdot s^{-1}$, longer half-life of 30-40 μs, and wider working pH range [1,2]. The sulfate radicals can be produced from persulfate (PS) or peroxymonosulfate (PMS) by different ways of activation, such as light, temperature, sonication, transition metal, and heterogeneous photocatalysis. Among them, photocatalytic activation is widely used due to its high effectiveness, low cost, non-toxicity, and low energy consumption [3].

Graphitic carbon nitride (g-C_3N_4) is structurally similar to graphene, consisting of several layers stacked along the axis to form graphite faces. The triazine rings C_3N_3, which are the structural units of graphite face, are bound together by element N. In addition, MIL-53(Fe) with the chemical formula of $Fe_3(OH)(O_2C\text{-}C_6H_4\text{-}CO_2)\cdot H_2O$ consists of FeO_6 octahedral chains connected with benzene dicarboxylate anions to form a 3-D network. This is a durable type of metal organic framework (MOFs) material with a large specific surface area, high adsorption capacity, and order structure, which is under intense research.

Both g-C_3N_4 and MIL-53(Fe) show a good ability to decompose pollutants under visible light. They are also environmentally friendly materials that can be easily synthesized in large quantity for practical applications. However, both pure g-C_3N_4 and MIL-53(Fe) have large photo-excited electron-hole recombination. To overcome this disadvantage, materials are often modified by doping with metals, nonmetals, or by hybridization between g-C_3N_4 and MIL-53(Fe) and other materials. Many studies have shown that the combination of g-C_3N_4 and MIL-53(Fe) materials has much better photochemical efficiency than the starting materials. Bai et al. [4] successfully synthesized g-C_3N_4/MIL-53(Fe) composite material to photocatalytically split H_2 from water under sunlight. The results showed that modified materials with the ratio g-C_3N_4/MIL-53(Fe)=1 : 1 had the highest H_2 splitting rate, which was 335 times and 47 times higher than those of MIL-53(Fe) and g-C_3N_4, respectively. The Cr(VI) removal efficiency in the water of g-C_3N_4 (3 wt%) doped MIL-53(Fe) was studied by Huang et al. [5]. Under the same conditions, the

†To whom correspondence should be addressed.
E-mail: nguyentrungdung1980@gmail.com, nnhuy@hcmut.edu.vn
Copyright by The Korean Institute of Chemical Engineers.

doped material had 3.4 and 4.8 times faster Cr(VI) removal rate than g-C_3N_4 and MIL-53(Fe), respectively. Co (1 wt%) doped g-C_3N_4 gave Rhodamine B (RhB) decomposition efficiency of four times higher than pure g-C_3N_4 [6]. The antibiotic degradation capacity of Ag_3PO_4/MIL-53(Fe) was studied by Xie et al. [7]. The results showed that Ag_3PO_4/MIL-53(Fe) material had better treatment efficiency than pure Ag_3PO_4 and MIL-53(Fe). With the ratio of Ag_3PO_4 : MIL-53(Fe)=1 : 3 (wt), the catalyst gave the highest degradation efficiency of tetracycline (93.72%), oxytetracycline (90.12%), chlortetracycline (85.54%), and deoxytetracycline (91.74%) within 1 h [7]. However, the combination of g-C_3N_4 and MIL-53(Fe) as an effective photocatalyst for photocatalytic degradation of RhB under visible light conditions has not been reported in the literature.

In this study, g-C_3N_4/MIL-53(Fe) material was synthesized by the hydrothermal method. The characteristics of the material were then determined by various techniques of surface analysis. The photocatalytic ability of the materials was then evaluated via its performance for the removal of RhB in water. The influencing factors such as type of catalyst, catalytic content, input RhB concentration, oxidant content, and pH condition were investigated. Finally, the mechanism for photocatalytic decomposition of RhB by g-C_3N_4/MIL-53(Fe) under visible light conditions was proposed.

MATERIALS AND METHODS

1. Preparation and Characterization of g-C_3N_4/MIL-53(Fe) Materials

The g-C_3N_4 material in this study was synthesized by the heat condensation method according to Wang et al. [8]. In a typical procedure, 10 g of melamine was finely ground and wrapped with aluminum foil. The material was then calcined at 525 °C for 3 h at a heating rate of 5 °C/min. After cooling to room temperature, the resulting yellow powder was g-C_3N_4. After that, the MIL-53(Fe) and g-C_3N_4/MIL-53(Fe) materials were synthesized by the hydrothermal method [5]. At first, 0.1105 g of g-C_3N_4 was mixed with 10 mL of N,N-Dimethylformamide (DMF), and the mixture was ultrasonically treated for 30 min to obtain solution A. Meanwhile, 2.703 g of $FeCl_3 \cdot 6H_2O$ and 1.66 g of H_2BDC were mixed with 56 mL of DMF for 20 min to obtain solution B. Solution A was then slowly added to solution B and the mixture was stirred for 1 h to obtain a homogeneous mixture (solution C). Next, solution C was transferred into a 100-mL autoclave for hydrothermal treatment at 150 °C for 24 h. The mixture was subsequently allowed to cool to room temperature before washing and filtration with DMF (3 times) and ethanol (3 times). The resulting solid was further soaked in 250 mL of DI water and stirred for 8-10 hours. Finally, the powder obtained after centrifuging and decantation was dried at 150 °C for 12 h. The final product following the above procedure was g-C_3N_4/MIL-53(Fe) with 97 wt% of MIL-53(Fe) and denoted as CNFe-97. The CNFe-99, CNFe-95, and CNFe-90 materials were synthesized using the same procedure but with different amounts of MIL-53(Fe). The chemicals used in this study come from China with 99% purity.

Characteristics of the synthesized materials were analyzed by various surface analyses. X-ray diffraction (XRD) patterns were collected using a D8 Advance XRD (Bruker, Germany). Fourier-transform infrared spectroscopy (FTIR) was analyzed by a Spectrum Two FT-IR Spectrometer (Perkin Elmer, USA) using attenuated total reflection (ATR) mode. Results of scanning electron microscopy (SEM) and energy-dispersive X-ray spectroscopy were obtained from an S-4800 FESEM (Hitachi, Japan). Brunauer-Emmett-Teller (BET) N_2 adsorption and desorption isotherms as well as pore size distribution were determined using a TriStar II Plus 2.03 (Micromeritics, USA). The UV-Vis absorption spectra using diffuse reflectance spectroscopy (DRS) were collected on a V-670 Spectrophotometer (Jasco, Japan). X-ray photoelectron spectroscopy (XPS) was performed using VG Multilab 2000 (Thermo Fisher Scientific, USA).

2. Photocatalytic Decomposition of Rhodamine B

The capability and applicability of the synthesized materials were evaluated by the photocatalytic decomposition of RhB in water (Fig. S1 of the Supplementary Material). Before performing the Rhodamine B decomposition experiment, the catalytic materials were treated in nitrogen gas for 12 h at 150 °C to clean the surface of the materials. In a batch reaction, 150 mL of water containing a certain RhB concentration according to each experiment was prepared in a double layer glass beaker with circulating water for stabilizing temperature. The photocatalyst was then added at a certain dosage depending on the test purpose. The mixture was stirred in dark conditions for 30 min to reach the adsorption equilibrium. Next, $Na_2S_2O_8$ was added with a certain concentration as an oxidizing agent in the experiment. The reaction was observed for 50 min under stirring by aeration. The light was turned on or off depending on the purpose of the experiment. The light was supplied by L4X LEDs (40 W, 12 V) with the highest intensity at a wavelength of 446 nm. RhB concentration was determined by UV-Vis absorption at a wavelength of 554 nm using a UV-Vis spectrophotometer (Model SP-60, Biochrom, UK) with 1.0 cm matched quartz cells. In the first experiments without the best-operating conditions, the values for RhB concentration, catalyst amount, $Na_2S_2O_8$ content, and pH were initially chosen at 20 mg/L, 300 mg/L, 200 mg/L, and 3, respectively. The photocatalyst used was g-C_3N_4/MIL-53(Fe) with 97% of MIL-53(Fe).

The RhB removal efficiency (H, %) and is the rate constant (k_{app}, min^{-1}) of the fitted pseudo-first-order kinetic model are calculated as follows:

$$H(\%)=(1-C_t/C_o)\times 100 \quad (1)$$

$$\ln(C_t/C_0)=k_{app}\times t \quad (2)$$

where C_0 and C_t (mg/L) are RhB concentration at the beginning and after reaction time, respectively.

To propose the mechanism of decomposition RhB by g-C_3N_4/MIL-53(Fe), the experiment to investigate the effects of free oxidizing radicals was conducted. The inhibition of free radicals was accomplished by adding 1 mM solution of ethylene diamine tetraacetic acid (EDTA-2Na), 1,4-benzoquinone (BQ), tert-butyl alcohol (TBA), or phenol (PheOH) to the solution before turning on the light.

To evaluate the reusability of the material, the catalyst was collected after each run. After that, the material was centrifuged, washed with distilled water twice and ethanol. The material was then dried at 70 °C and applied for the next experiment.

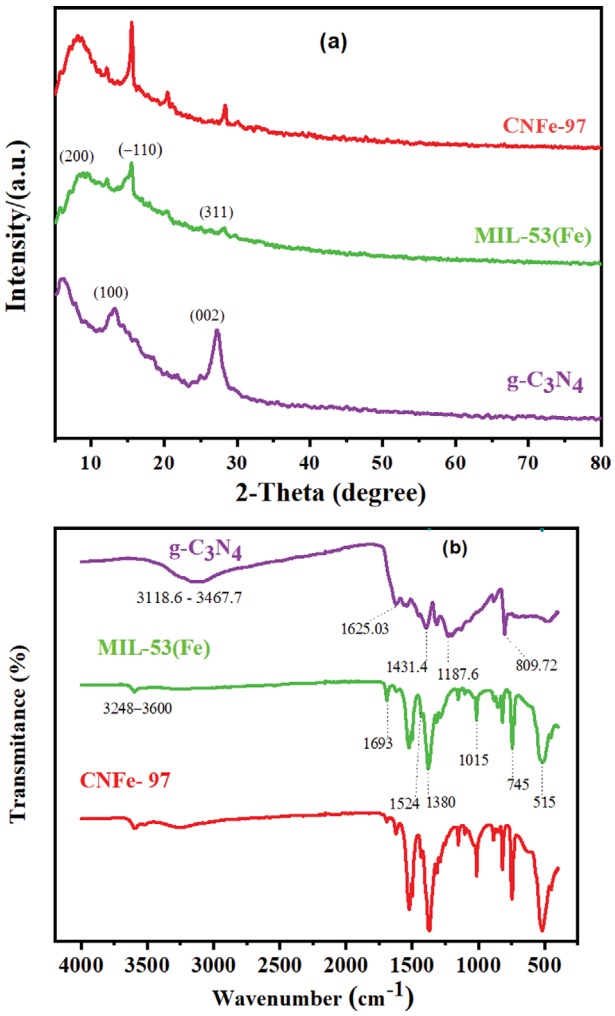

Fig. 1. (a) XRD patterns and (b) FT-IR spectra of g-C_3N_4, MIL-53(Fe), and CNFe-97.

RESULTS AND DISCUSSION

1. Material Synthesis and Characterization

XRD patterns were used to determine the crystalline structure of g-C_3N_4, MIL-53(Fe), and CNFe-97 with 2θ in the range of 2-80° (Fig. 1(a)). The XRD spectrum of g-C_3N_4 has two high-intensity peaks at 13.15° and 27.25°, which can be explained by the cyclic arrangement of tri-s-triazine units in the plane (100) (2θ=13.15°) and the arrangement of plane-corresponding aromatic conjugation systems (002) (2θ=27.25°). This result is consistent with the published work on the phase composition of g-C_3N_4 [8,9]. Peaks characteristic for MIL-53(Fe) material are observed at 2θ of 9.17°, 17.33°, and 25.22°, corresponding to the planes of (200), (-110), and (311), respectively [10,11]. The XRD spectrum of CNFe-97 has the same diffraction peaks as MIL-53(Fe). Meanwhile, the characteristic peaks of g-C_3N_4 are not observed, mostly due to the small content of g-C_3N_4 (3 wt%) in the composition of composite material. The enhancement of characteristic peaks at 2θ of 17.33° and 25.22° in CNFe-97 as compared to those in MIL-53(Fe) materials is attributed to the weak interaction of amine groups on the surface of g-C_3N_4 with Fe atoms in MIL-53(Fe), which improves the crystallinity of MIL-53(Fe) material [12]. The crystal structure of MIL-53(Fe) did not change when adding g-C_3N_4, which is also consistent with the reports of Bai et al. [4] and Huang et al. [5]. Thus, it can be concluded that the g-C_3N_4, MIL-53(Fe), and CNFe-97 materials were successfully synthesized with high purity.

FTIR spectra of g-C_3N_4, MIL-53(Fe), and CNFe-97 are shown in Fig. 1(b) with wavenumbers in the range of 400-4,000 cm^{-1}. FTIR spectrum of g-C_3N_4 has an adsorption peak at 810 cm^{-1}, which can be attributed to the C-N bond in the aromatic ring. Some peaks in the range of 1,188-1,431 cm^{-1} with high intensity are also ascribed to be the vibration of the C-N bond outside the aromatic ring. The peak at 1,625 cm^{-1} is the vibration due to the C=N bond. Wide adsorption bands in the range of 3,118-3,467 cm^{-1} are the vibration of the secondary and primary amines due to the formation of hydrogen bonds between their molecules. This is because the hydrogen atoms are also bound to C-N in the aromatic ring as well as to the C-NH_2 and C-NH-C groups in the graphene-like structure of g-C_3N_4 [8,9]. MIL-53(Fe) material has some peaks at wavenumbers of 1,693 cm^{-1} (the vibration of the C=O bond), 1,524 and 1,380 cm^{-1} (symmetric and asymmetric stretching of the carboxylate group), 515 cm^{-1} (the vibration of Fe-O bonding in octahedral FeO_6), 745-1,015 cm^{-1} (the C-H bonding vibration of the benzene ring), and 3,248-3,600 cm^{-1} (the existence of O-H groups in the structure) [10,11]. Similar to XRD patterns, FTIR spectra results also show that doping g-C_3N_4 does not affect the basic functional groups in MIL-53(Fe). The characteristic peaks in the FTIR spectrum of CNFe-97 coincide with those in MIL-53(Fe).

As shown in Fig. 2(a), MIL-53(Fe) morphology has a rod shape with a smooth surface and irregular sizes. This result is similar to

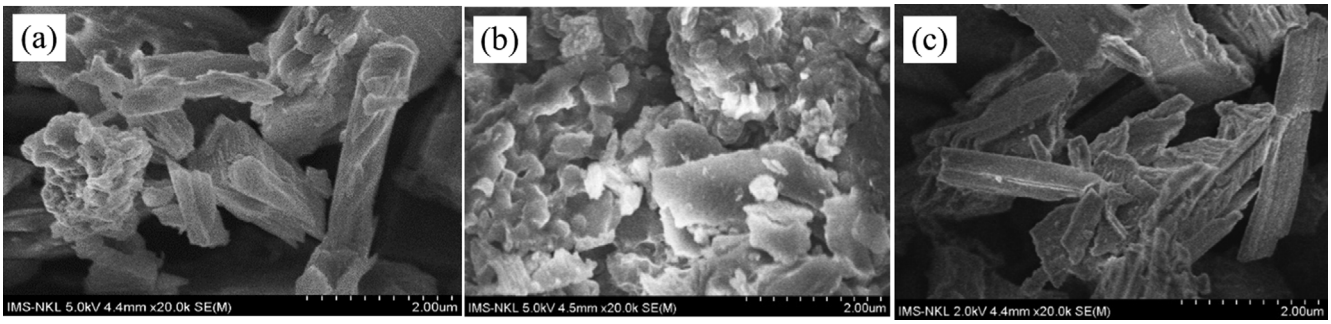

Fig. 2. SEM images of (a) MIL-53(Fe), (b) g-C_3N_4, and (c) CNFe-97.

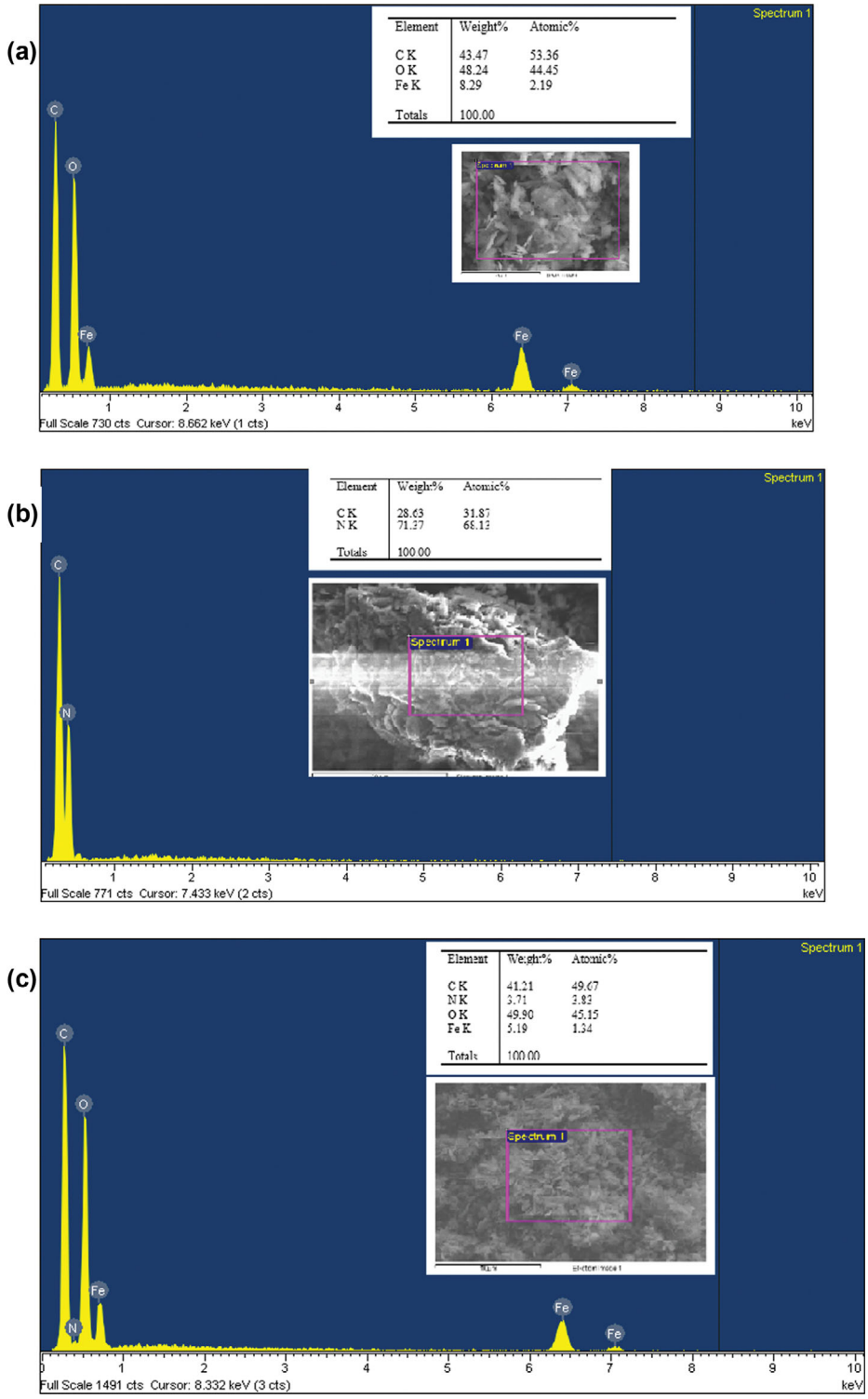

Fig. 3. EDX spectrum of (a) MIL-53(Fe), (b) g-C_3N_4, and (c) CNFe-97.

the study of Salimi et al. [13]. The morphology of pure g-C_3N_4 material (Fig. 2(b)) is unevenly stacked, as reported in previous studies [5,14]. The morphology of CNFe-97 (Fig. 2(c)) is similar to that of MIL-53(Fe), but the surface is somewhat rougher, which could be due to the adhesion of g-C_3N_4 on the CNFe-97 surface.

EDX spectra of g-CN_3N_4, MIL-53(Fe), and CNFe-97 are shown in Fig. 3. There are signals which are specific to the elements of Fe (2.19%), C (44.45%), and O (53.36%) in the MIL-53(Fe) material. Thus, it is possible to determine that the main components in the MIL-53(Fe) are C and O, proving that the material has been successfully synthesized [11,15]. Meanwhile, g-C_3N_4 is also successfully synthesized when the elements of C and N predominantly

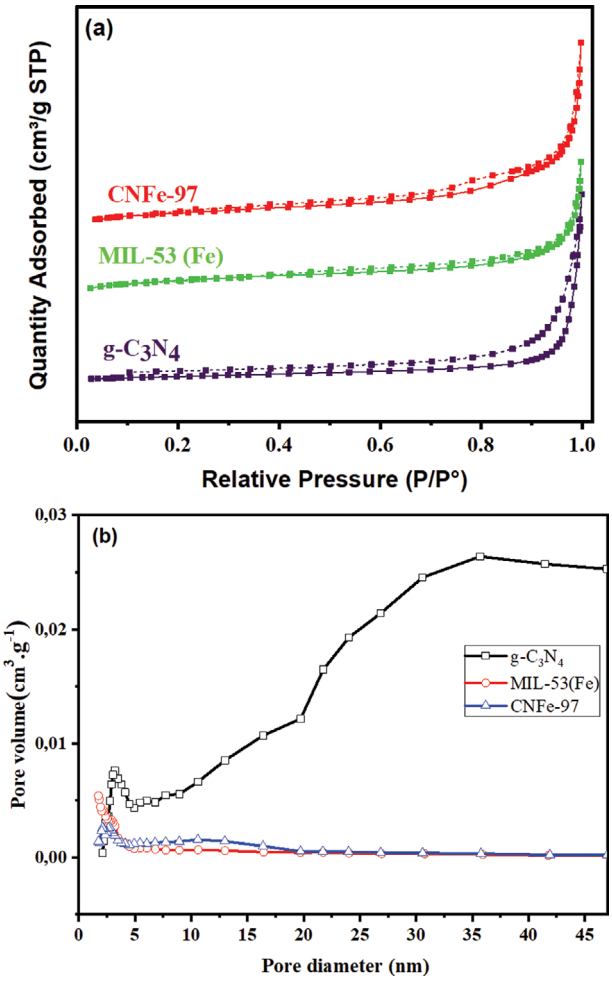

Fig. 4. (a) N_2 adsorption-desorption isotherms, and (b) pore size distribution of MIL-53(Fe), g-C_3N_4, and CNFe-97.

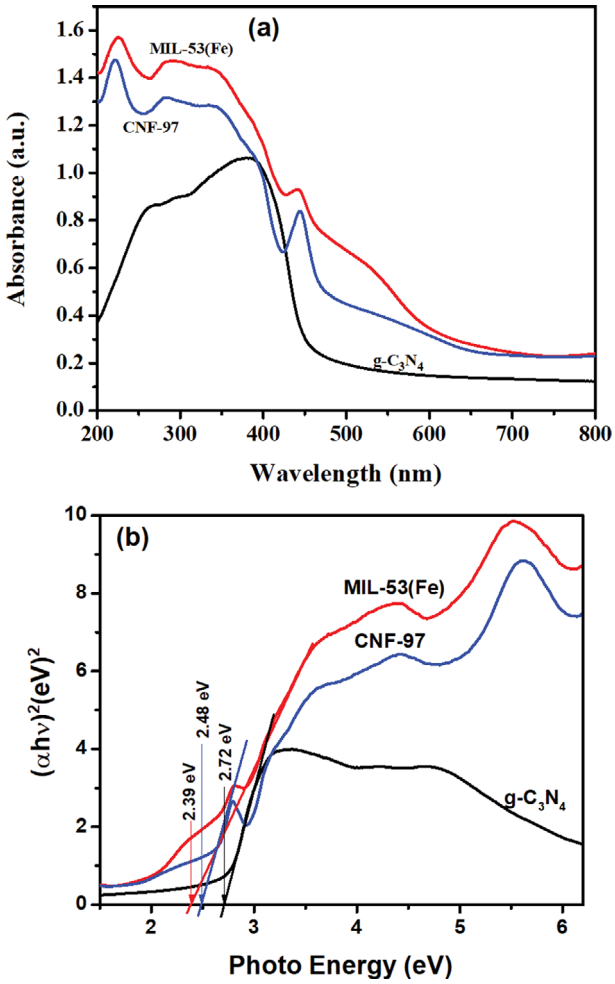

Fig. 5. (a) UV-Vis DRS spectrum of materials and (b) the plot of $(\alpha h\nu)^2$ vs. photo energy ($h\nu$).

appear with high percentages of 31.87% and 68.13%, respectively, which is similar to previous reports [16,17]. EDX spectrum of CNFe-97 indicates the presence of the main elements such as Fe, N, C, and O. These results together with the SEM images confirm that g-C_3N_4 was successfully doped into the MIL-53(Fe) material.

As observed from Fig. 4(a), the N_2 adsorption-desorption isotherms of MIL-53(Fe), g-C_3N_4, and CNFe-97 are all of type IV according to IUAPC [18]. In addition, Fig. 4(b) shows the pore size distribution of these materials, while some porous parameters of materials from BET analysis results are summarized in Table 1. MIL-53(Fe) has a surface area of 25.55 m^2/g and an average pore size of 8.05 nm. Those values are similar to those reported in the literature with a surface area of 14 m^2/g [19], 20.6 m^2/g [20], 26.20 m^2/g [21], and 19.1-89.69 m^2/g [22], and pore size of 5.6 nm [21]. However, the very low surface area observed on MIL-53(Fe) indicates that the anhydrous form of MIL-53(Fe) exhibits closed pores and decreased capillary sizes, which are smaller than the kinetic diameter of N_2 at 77 K. Therefore, nitrogen cannot reach these capillaries, resulting in a reduced specific surface area [18,19,23]. In this study, g-C_3N_4 has an area surface of 6.96 m^2/g and pore size of 35.7 nm, which are higher than the values of 4.31 m^2/g and 14.6 nm in the study of Shanmugam et al. [24]. Compared with MIL-53(Fe), CNFe-97 has a smaller specific surface area (19.16 vs. 25.55 m^2/g) but higher pore volume (0.068 vs. 0.051 cm^3/g), which was caused by the attachment of g-C_3N_4 on the surface of MIL-53(Fe).

Table 1. BET results of the synthesized materials

Materials	Surface area (m^2/g)	Pore size (nm)	Pore volume (cm^3/g)
MIL-53(Fe)	25.55	8.05	0.051
g-C_3N_4	6.96	35.7	0.06
CNFe-97	19.16	14.21	0.068

The results from the UV-Vis absorption of the synthesized materials are illustrated in Fig. 5. As seen in Fig. 5(a), g-C_3N_4 has absorption peaks at 273 nm and 380 nm, proving its working ability under visible light conditions. Similarly, MIL-53(Fe) has absorption peaks at 230 and 441 nm, which is capable of absorbing visible light in the wavelength range of 400-600 nm. At the wavelength of 441 nm, MIL-53(Fe) spectrum is specific to the O-Fe-O bond. The absorption spectrum of CNFe-97 shows a similarity to the MIL-53(Fe) spectrum with an absorption wavelength at 448 nm,

which was shifted towards a longer wavelength than that of MIL-53(Fe). The UV-Vis DRS results were applied to determine the bandgap energy of the g-C_3N_4, MIL-53(Fe), and CNFe-97 materials (Fig. 5(b)), which are 2.72, 2.39, and 2.48 eV, respectively. This is one of the important bases for proposing a photocatalytic mechanism with CNFe-97.

X-ray photoelectron spectroscopy (XPS) was conducted to investigate the surface composition and elemental valence state in the g-C_3N_4/MIL-53(Fe) composite. The full-scan XPS spectrum (Fig. 6(a)) shows the existence of O1s at 532 eV, C1s at 284 eV, N1s at 399 eV, and Fe2p at 712 eV elementals [25]. The C1s spectrum (Fig. 6(b)) can be deconvoluted into five components referring to C=C/C-C (284.8 eV), C=O (286.2 eV), C=O (288.9 eV), O-C=O (290.8 eV), sp^2-bonded carbon (N=C-N, 248.8 eV), and graphitic carbon (sp^3 C, 285.6 eV) groups [25-27]. The N1s spectrum (Fig. 6(c)) can be fitted using three components referring to sp^2 N (C-N=C, 398.8 eV), tertiary N atoms (sp^3 N, 399.9 eV), amino-functional groups (C_2-N-H, 401.0 eV) groups [28]. The high-resolution O1s has three peaks (Fig. 6(d)), which can be classified as lattice oxygen in the bond between metal and oxygen (Fe-O), chemisorbed oxygen species, and oxygen in O-C=O groups [19,29,30]. Two peaks of Fe2p allocated at 712.3 eV and 726 eV for Fe 2p1/2 and Fe 2p3/2 (Fig.

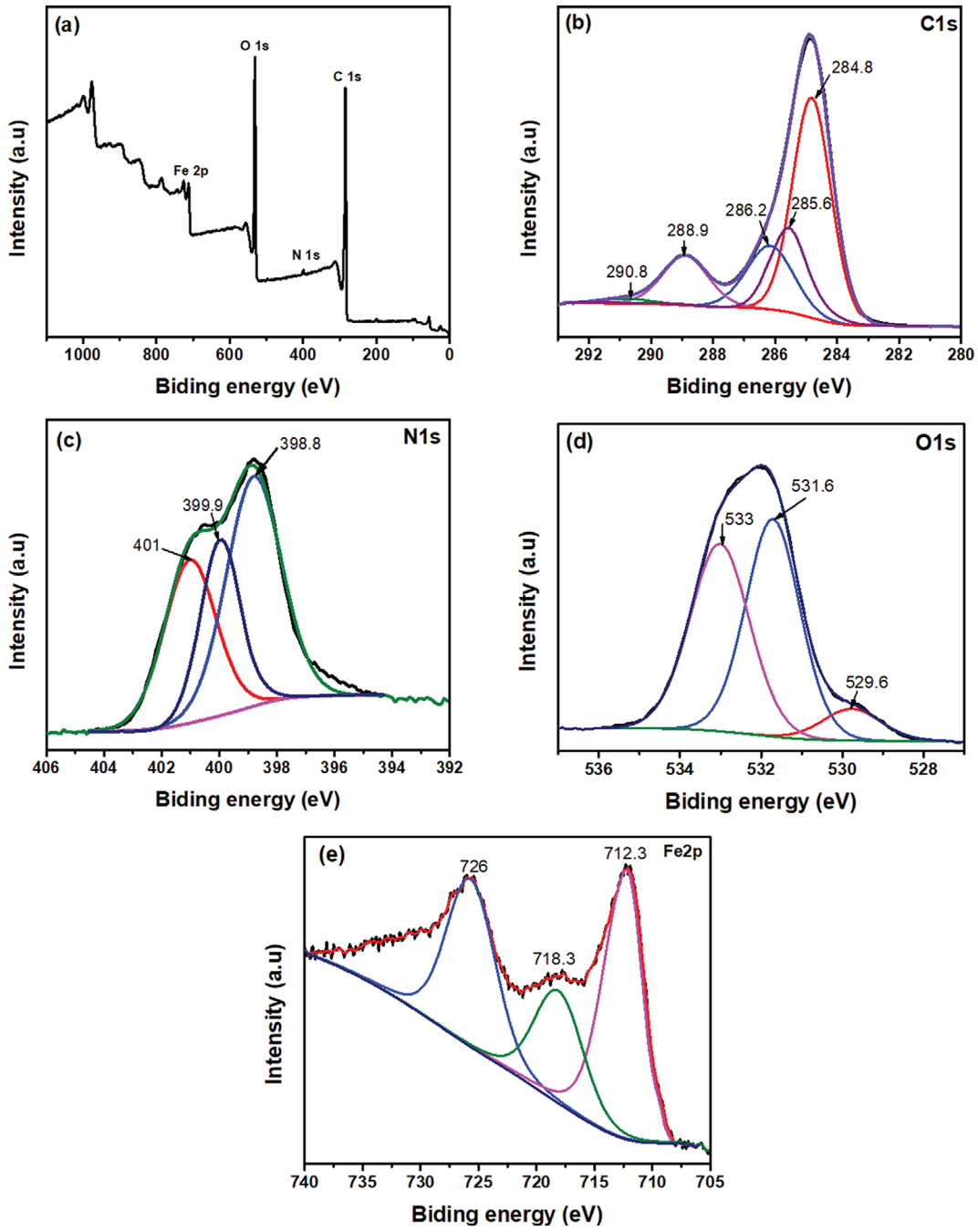

Fig. 6. XPS results of g-C_3N_4/MIL-53(Fe): (a) Survey scan, (b) C1s peak, (c) N1s peak (d) O1s peak, and (e) Fe2p peak.

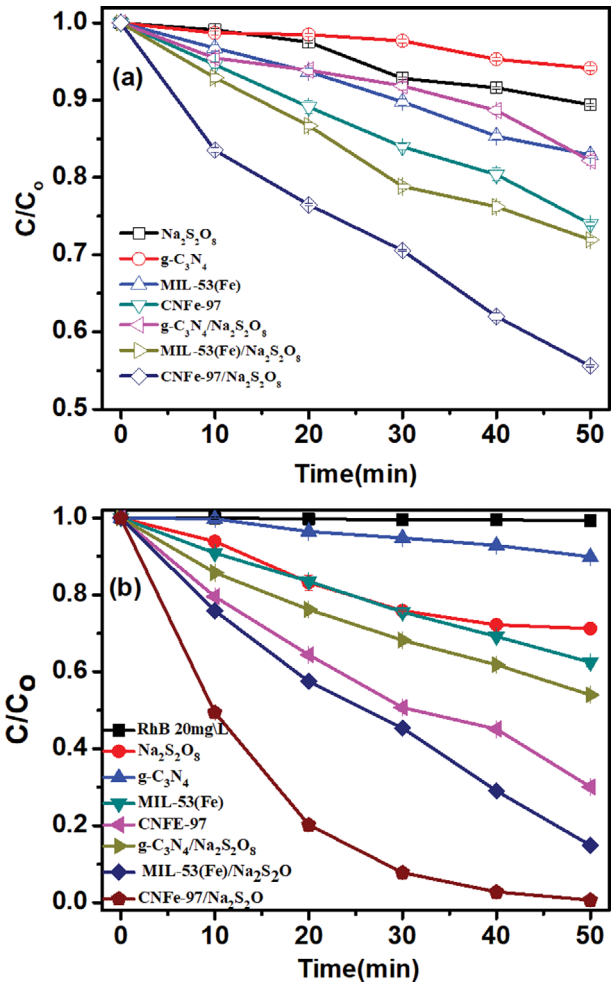

Fig. 7. Removal of RhB without (a) and with (b) light illumination.

6(e)) were both observed in g-C_3N_4/MIL-53(Fe) composite [31]. There is also a peak with a satellite signal at 718.3 eV, confirming that Fe(III) exists in the MIL-53(Fe) structure [25,31]. The XRD and XPS results show that g-C_3N_4/Mil-53(Fe) material was successfully synthesized.

2. Photocatalytic Removal of Rhodamine B

At first, the effects of illumination, the presence of $Na_2S_2O_8$, and catalyst on RhB removal efficiency were observed. The results in Fig. 7 show that these factors remarkedly affect the degradation of RhB in water with greater efficiency in the presence of light, $Na_2S_2O_8$, and photocatalyst. In the absence of light and photocatalyst, the RhB removal by $Na_2S_2O_8$ was only 10.70% after 50 min of reaction. Without light and $Na_2S_2O_8$, the RhB treatment efficiency by adsorption was very low at 5.94%, 17.46%, and 26.23% for g-C_3N_4, MIL-53(Fe), and CNFe-97, respectively. Without light, the combination of catalysts and $Na_2S_2O_8$ gave slightly higher removal efficiency of 17.7%, 27.23%, and 44.36% with g-C_3N_4, MIL-53(Fe), and CNFe-97, respectively. Various oxidants ($Na_2S_2O_8$, $K_2S_2O_8$, $(NH_4)_2S_2O_8$, H_2O_2, $KHSO_5$ (PMS), and KIO_3) were also applied for the treatment of RhB, and $Na_2S_2O_8$ was proven to be the best oxidant for the photocatalytic removal of RhB in water (Fig. S2 of the Supplementary Material). The presence of $Na_2S_2O_8$ increases RhB decomposition because it enhances the electron transfer in the catalytic reaction, which is similar to the research of Huang et al. [5].

In the case of illumination, the photolytic decomposition of RhB did not take place in the absence of $Na_2S_2O_8$ and catalyst. When adding an oxidizing agent, the RhB removal efficiency reached 27.81%, which was higher than that of the non-illuminated experiment (10.70%). However, the use of $Na_2S_2O_8$ for direct oxidation of RhB is still not effective. Under light illumination conditions, the catalysts gave better removal efficiency than in the absence of light, reaching 10.1%, 38.47%, and 69.51% with g-C_3N_4, MIL-53(Fe), and CNFe-97, respectively. In the presence of all three elements (light, oxidizing agent, and catalysts), the RhB removal efficiency was significantly increased. In which, CNFe-97 achieved the highest efficiency of 99.35%, followed by MIL-53(Fe) with efficiency of 85.11%. The calculated results show that the RhB decomposition rate of CNFe-97 (0.0994 min^{-1}) is 7.46 times higher than that of g-C_3N_4 (0.0126 min^{-1}) and 2.75 times higher than that of MIL-53(Fe) (0.0361 min^{-1}).

Thus, the photocatalytic ability of the CNFe-97 composite material is superior to that of pure g-C_3N_4 and MIL-53(Fe), especially in the presence of the oxidizing agent ($Na_2S_2O_8$) for RhB removal. Regarding pure g-C_3N_4, although it has a narrow bandgap of ~2.72 eV, it has weak photocatalytic activity. This is possibly due to its high electron-hole recombination, which leads to a decrease in photocatalytic efficiency. In the case of MIL-53(Fe) or CNFe-97, the e^-/h^+ recombination is limited, likely because of its rod morphology, which improves the RhB treatment efficiency. In addition, g-C_3N_4 doping improves the ability to trap electrons, therefore helps to limit the electron-hole recombination and make the higher RhB removal efficiency of CNFe-97 as compared to that of MIL-53(Fe).

In this experiment, the influence of g-C_3N_4 content on the activity of g-C_3N_4/MIL-53(Fe) for RhB removal was investigated. The MIL-53(Fe) content of photocatalysts was varied in the range of 90-100 wt%, including CNFe-90, CNFe-95, CNFe-97, CNFe-99, and CNFe-100 (MIL-53(Fe)). The result in Fig. 8(a) shows that when increasing the content of g-C_3N_4 from 0 to 3 wt%, the photocatalytic efficiency increases from 85.11% to 99.35%. However, the treatment performance of RhB then decreases with a further increase of g-C_3N_4 content from 3 to 10 wt%, where the CNFe-90 only reaches a removal efficiency of 79.53%. This is probably because the electron and hole separation efficiency is improved under moderate content of doped g-C_3N_4 due to the effective electron transfer. If the g-C_3N_4 content continues to increase, g-C_3N_4 would deposit densely on the photocatalyst surface, which hinders the contact between light and MIL-53(Fe). In addition, g-C_3N_4 could also turn into the centers for the e^-/h^+ recombination under high content, which is consistent with the statement of Gong et al. [32]. Under the same lighting conditions and $Na_2S_2O_8$, CNFe-97 gave the highest treatment efficiency of 99.35% after 50 min of reaction with the RhB decomposition rate of 1.67 to 3.21 times faster than other catalysts (Fig. 8(b)). The change in RhB concentration over time followed the first-order equation with $R^2 \geq 0.957$ (Fig. 8(b)). Therefore, CNFe-97 was selected as the photocatalyst in the subsequent experiments with $Na_2S_2O_8$ and light presence. UV-Vis molecular absorption spectrum of RhB when using CNFe-97 and $Na_2S_2O_8$ presence over time is observed in Fig. 8(c). The results show that

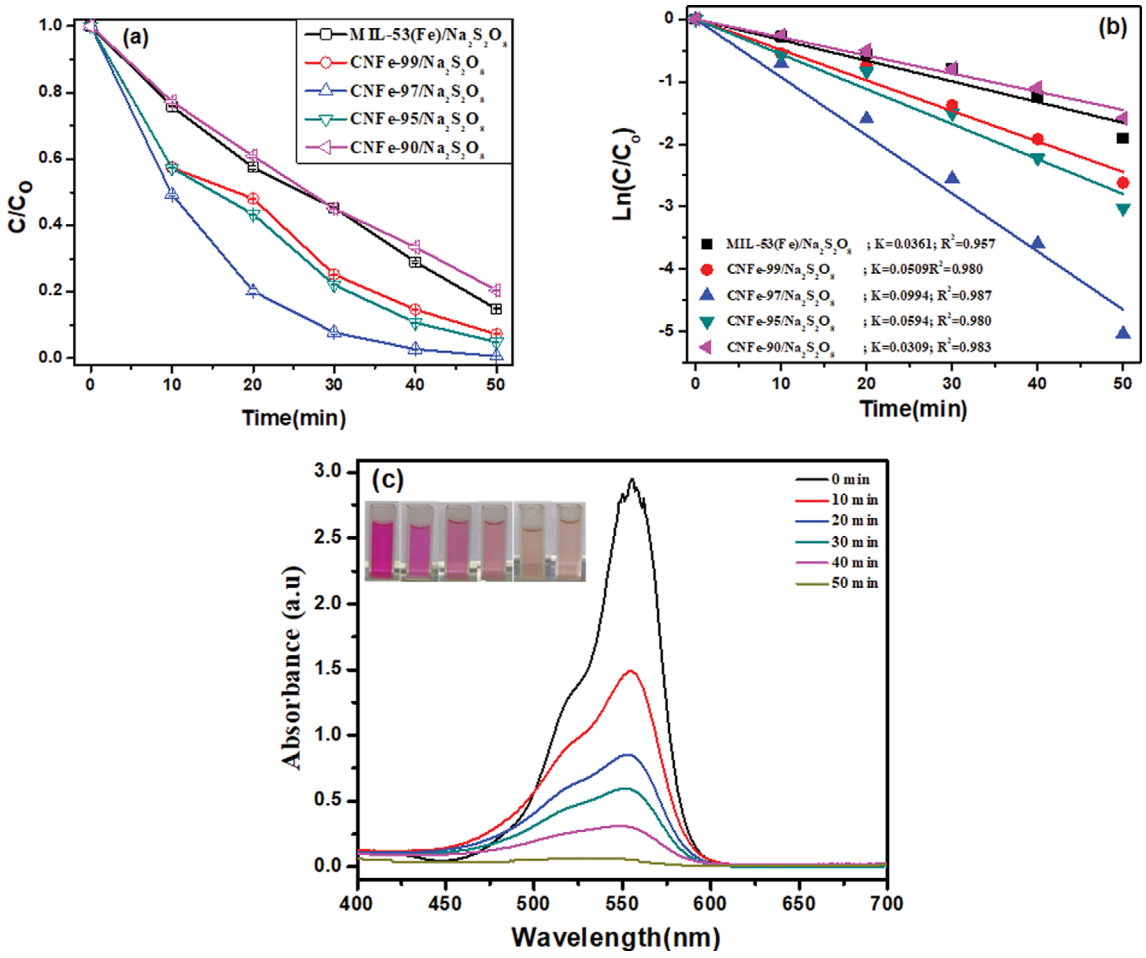

Fig. 8. (a) Effect of g-C_3N_4 content on the RhB removal efficiency of CNFe, (b) Kinetic of removal RhB by CNFe-x (with x=90, 95, 97, 99, or 100), and (c) spectral absorption of RhB UV-Vis molecule over time.

over time, there was not any wavelength shift of the peak of 554 nm that can be observed. Meanwhile, the absorption intensity changed rapidly after the first 10 min of reaction and the spectral peak almost disappeared completely after 50 min. This indicates that CNFe-97 effectively activates oxidizing agent $Na_2S_2O_8$ to stimulate the process of creating free radicals for the decomposition of RhB under visible light conditions.

The used amount of the catalyst usually affects not only the treatment efficiency but also the cost of a photocatalytic process. Therefore, the determination of suitable photocatalyst dosage is an important step for water treatment. In this experiment, CNFe-97 was used in a dosage range of 50-500 mg/L. As presented in Fig. 9, the RhB decomposition process followed first-order kinetics at all different photocatalyst dosages with $R^2 \geq 0.970$. When increasing the photocatalyst dosage from 50 to 300 mg/L, the removal efficiency after 50 min increased from 64.02 to 99.35% and the decomposition rate constant of RhB increased from 0.02 to 0.0994 min^{-1}. When the dosage increased, the photocatalysis would be increased with more holes (h^+) generated and more electrons (e^-) transferred, which enhances the formation of free radicals and increases the RhB decomposition. However, when the dosage increased from 300 to 400 and 500 mg/L, the rate constant and the efficiency of decomposition RhB did not change significantly, which could be due to the ineffective light contact under the high concentration of catalyst suspended in the solution. Therefore, we chose a catalyst content of 300 mg/L to conduct further experiments.

The initial concentration of reactant is an important factor that directly affects removal efficiency. In this experiment, the initial RhB concentration was changed in the range of 5-50 mg/L. Similar to the previous experiments, the RhB decomposition process complied with the first-order kinetic equation with $R^2 \geq 0.925$. The result in Fig. 10 shows that when the RhB concentration increased, the decomposition efficiency and rate of RhB decreased. Specifically, at low RhB concentration of 5 and 10 mg/L, the RhB removal efficiency reached almost 100% after 30 min. The RhB removal efficiency was also very high at 99.35% after 50 min of reaction at RhB concertation of 20 mg/L. The reaction rate constants were calculated to be 0.1411, 0.1104, and 0.0994 min^{-1} at RhB concentration of 5, 10, and 20 mg/L, respectively. Thus, in the low concentration range of RhB (5-20 mg/L), the removal efficiency and the rate constant of RhB did not change significantly. When increasing the RhB content to 30 and 50 mg/L, the efficiency after 50 min achieved 79.56% and 30.45%, respectively, with reaction rate constants of 0.031 and 0.0069 min^{-1}, respectively.

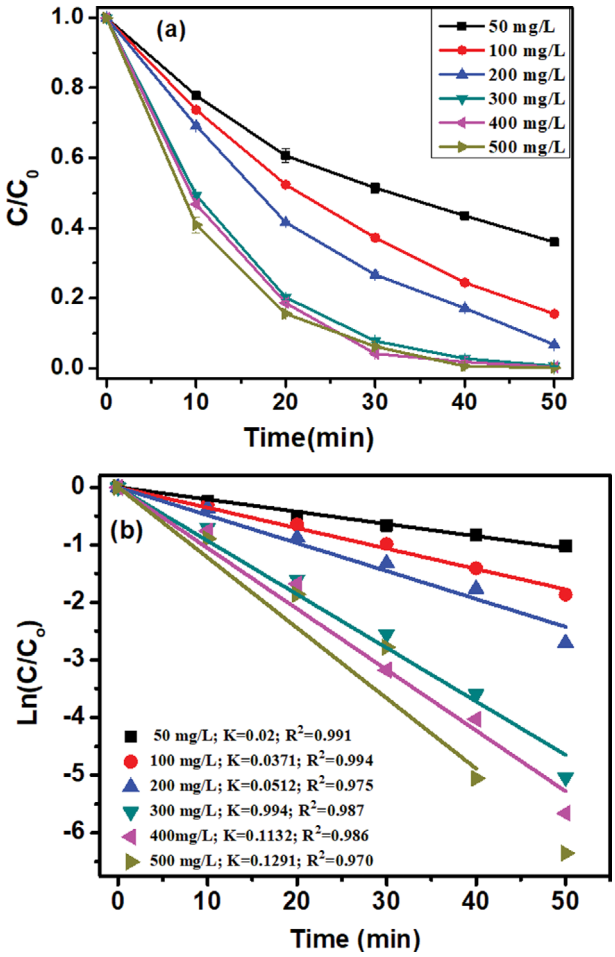

Fig. 9. (a) Effect of photocatalyst dosage on RhB removal and (b) kinetics of RhB removal at different photocatalyst dosages.

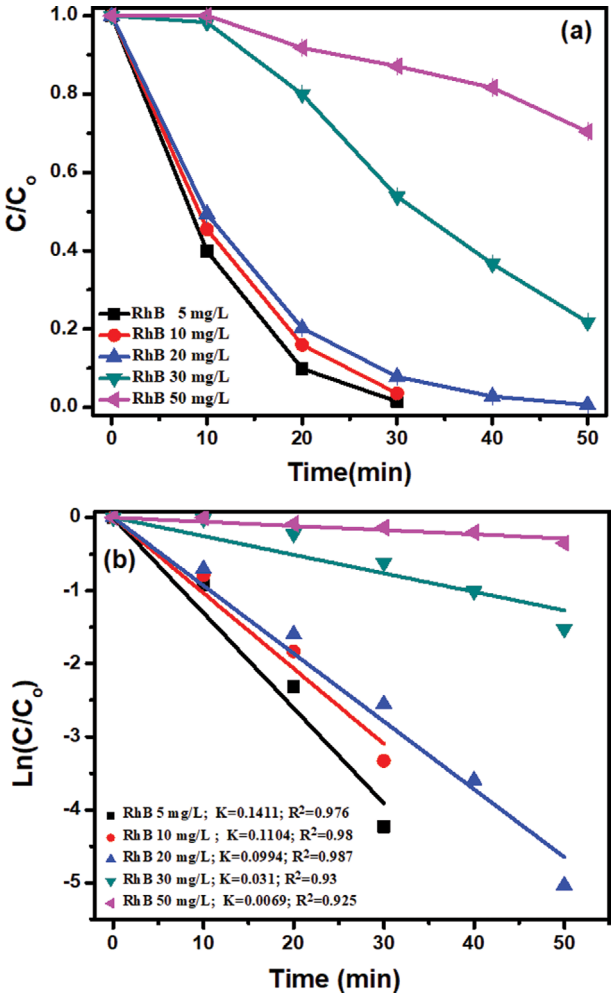

Fig. 10. (a) Effect of initial concentration of RhB and (b) kinetics of RhB removal at different initial RhB concentrations.

The photocatalytic decomposition rate depends on the formation of free radicals on the catalytic surface and the possible reactivity between these radicals and the RhB pollutant. When the initial content of RhB increases, a greater amount of RhB is adsorbed by the active centers on the surface of the CNFe-97catalyst and reduces the adsorption of $S_2O_8^{2-}$ on the catalytic surface. Hence, the rate of formation of free radicals (e.g., sulfate and hydroxyl) decreased, and therefore the decomposition efficiency of RhB decreased. On the other hand, according to Beer's law, the increase in RhB concentration prevents light transmission into the solution and the catalyst surface. Consequently, the absorption of photons by the catalyst is reduced, resulting in a reduced photocatalytic decomposition. Therefore, the RhB concentration of 20 mg/L was chosen for the next study to meet the requirements of treatment time and efficiency for other parameters.

Since the presence of $Na_2S_2O_8$ affects the RhB removal efficiency, the effect of $Na_2S_2O_8$ concentration was investigated in the range of 50-400 mg/L. As shown in Fig. 11, the RhB decomposition kinetics at different concentrations of $Na_2S_2O_8$ also followed the first-order kinetic equation with $R^2 \geq 0.97$. When increasing the $Na_2S_2O_8$ content, the RhB decomposition rate and efficiency both increased significantly. At a low $Na_2S_2O_8$ content of 50 mg/L, the RhB removal efficiency was only 64.62% after 50 min of reaction, which could be the insufficiency of $Na_2S_2O_8$ for the activation of persulfates to create free radicals. When increasing the $Na_2S_2O_8$ content from 100 mg/L to 200 mg/L, the RhB removal efficiency reached 85.09% and 99.35%, respectively, after 50 min and the reaction rate constant also increased from 0.0369 to 0.0994 min^{-1}. When increasing the $Na_2S_2O_8$ from 300 mg/L to 400 mg/L, the decomposition efficiency and the RhB decomposition rate constant did not change significantly. The reason is that excess persulfate content can react with sulfate radicals ($SO_4^{\bullet-}$) to form less oxidizing persulfate: $S_2O_8^{2-} + SO_4^{\bullet-} \rightarrow SO_4^{2-} + S_2O_8^{\bullet-}$. Therefore, in the range of $Na_2S_2O_8$ in 200-400 mg/L, the treatment efficiency of RhB did not change significantly. Based on the above experimental results, we used the $Na_2S_2O_8$ content of 200 mg/L for further experiments.

Since the surface property of the catalyst material changes with acidic - basic conditions, the pH of the solution is one of the important factors that affect the treatment efficiency of a photocatalytic process. The effect of solution pH on the RhB removal was studied in the range of 3-11 and the results are shown in Fig. 12, showing that pH significantly affects the RhB decomposition. The change of pH during the reaction time can be found in Fig. S3 of

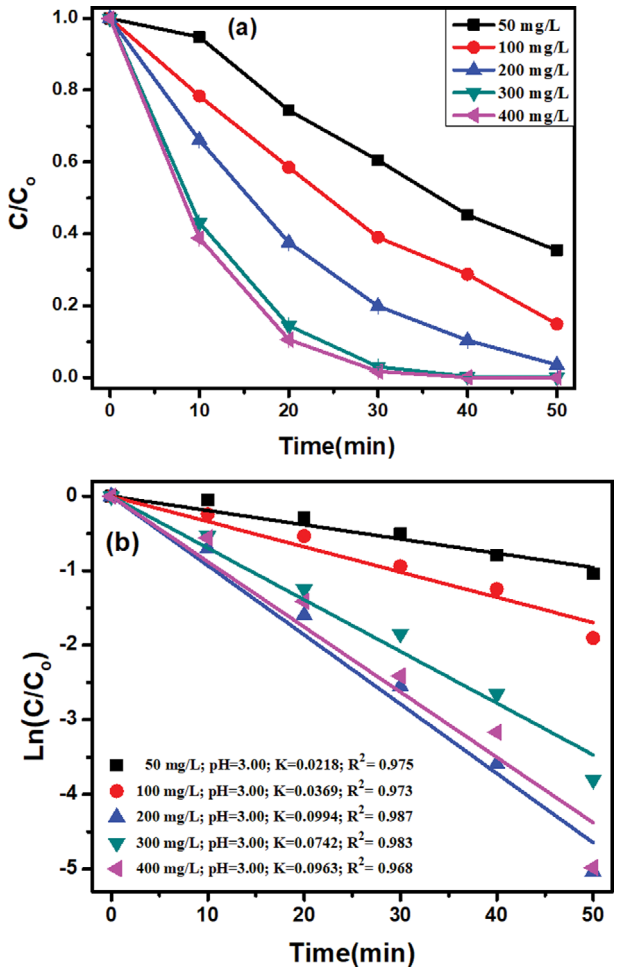

Fig. 11. (a) Effect of $Na_2S_2O_8$ content and (b) Kinetics of RhB removal at different $Na_2S_2O_8$ concentrations.

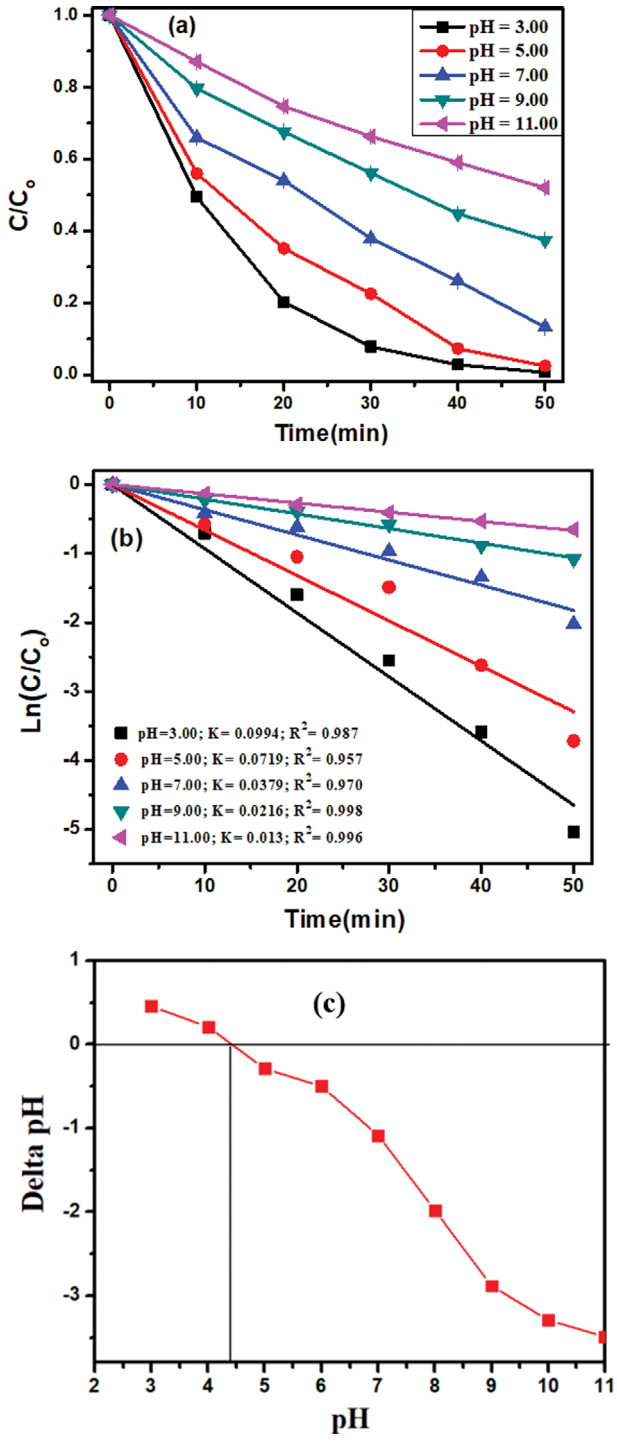

Fig. 12. (a) RhB removal efficiency in different pH conditions, (b) Kinetics of RhB removal at pH conditions, and (c) pH_{pzc} plot ($pH_f - pH_i$ vs. pH_i).

the Supplementary Material, showing a rapid pH decrease in the first 10 min and a slight decrease after that. The RhB both removal efficiency and removal rate constant decreased with the increase of pH from 3-11. Under strongly acidic conditions (pH 3), the RhB decomposition rate was the fastest with the removal of 99.35% and a constant rate of 0.0994 min^{-1}. At higher pH values, the RhB treatment efficiency began to decline and reached only 48.04% at pH 11. The pHzpc of the material was determined to be 4.42 (Fig. 12(c)). The tendency for the surface to be positively charged at low pH helps catalyst to easily interact with $S_2O_8^-$, which enhances the activation of free radicals and promotes photochemical processes. On the other hand, at pH 3, the reaction system may work as a Fenton-like reaction due to the formation of Fe^{2+} in solution from redox processes on the surface of the material [33,34]. In contrast, under alkaline conditions, the CNFe-97 material is weakened due to the unstable MIL-53(Fe), which reduces the catalytic activity. Hence, pH 3 was chosen for the next experiments.

In this experiment, the catalytic reusability was evaluated with five regeneration times by ethanol. CNFe-97 was used and the operating factors were the same as in previous experiments. The results in Fig. 13 show a decrease in the treatment capacity after regeneration of the photocatalytic material. Specifically, the efficiency decreased from 99.35% to 78.13% after five regeneration times. It can be concluded that the activity of the material is relatively stable and that the regeneration after use is feasible. The photocatalyst was also applied for the treatment of other dyes (DB-71, MB, and MO) to evaluate the ability of the catalyst. The results can be seen in Fig. S4 of the Supplementary Material, proving the applica-

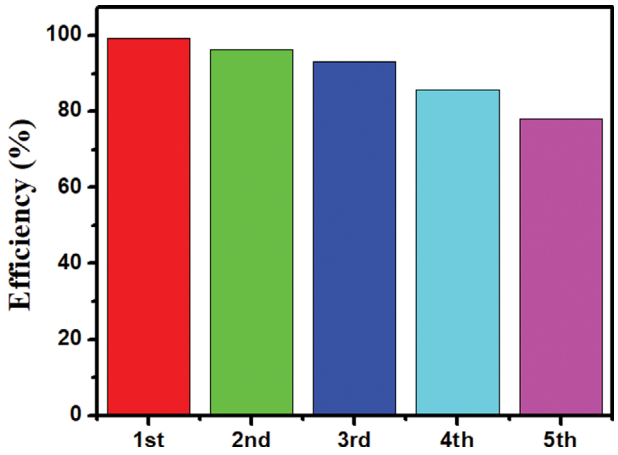

Fig. 13. RhB removal efficiency of CNFe-97 after 5 regeneration times.

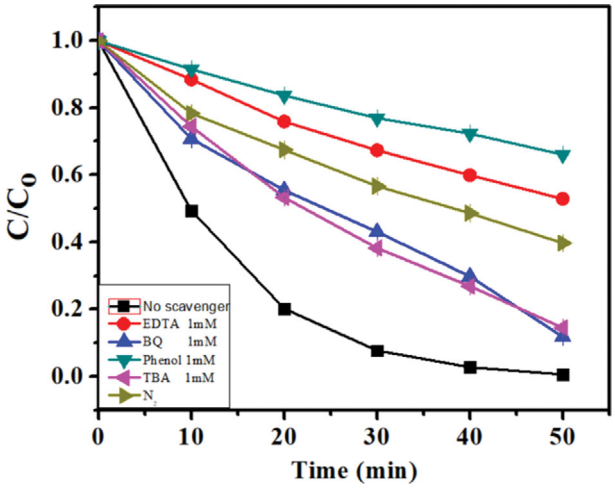

Fig. 14. Effect of extinguishing agents on RhB removal by the CNFe-97/$Na_2S_2O_8$.

bility of the catalyst in practical applications of textile wastewater treatment.

The comparison between g-C_3N_4/MIL-53(Fe) and other similar materials for sulfate activation under visible light is summarized in Table S1 of Supplementary Material. It was shown that the reactive oxidation species such as $SO_4^{\bullet-}$, $O_2^{\bullet-}$, $HO^{\bullet}$ and h^+ play an important role in the degradation of aqueous pollutants such as dyes (rhodamine B and methylene blue), antibiotics (tetracycline and levofloxacin), and bisphenol A. As compared to other catalytic materials, g-C_3N_4/MIL-53(Fe) (97%) in this study has an advantage for photocatalytic removal of organics in water such as low dosage of 300 mg/L, high efficiency of 99.35%, high pollutant concentration of 20 mg/L, high degradation rate of 0.094 min^{-1}, short reaction time of 50 min, and low persulfate dosage of 0.84 mM. Besides, the catalyst is made of environmentally friendly components (C, N, and Fe) and works under LED with low capital and operational cost, which is very promising for large-scale application in wastewater treatment.

3. Mechanism of Photocatalytic Removal of RhB by CNFe97

In photocatalytic reactions, free radicals can form in intermediate stages. Under the action of appropriate light, a photoexcited electron-hole pair will be formed and be the main cause of free radicals. Specifically, after the photo-excited electron-hole formation, they are transported to the surface of the material and in contact with the environment. Here, h^+ will participate in oxidation reaction with water to create free radicals $HO^{\bullet}$ where electrons will participate in reduction reaction with persulfate and oxygen to create free radicals such as $SO_4^{\bullet-}$ and $O_2^{\bullet-}$. These free radicals will play an important role in the decomposition of RhB. To determine the free radicals that form and play a decisive role in the decomposition of RhB by the CNFe-97/$Na_2S_2O_8$/visible light system, a series of experiments were conducted on free radical quenching experiments by organic matter such as EDTA-2Na, tert-butanol (TBA), 1,4-benzoquinon (BQ), and phenol (PheOH) at 1 mM concentrations. In which, EDTA-2Na is capable of extinguishing the activity of holes (h^+) and BQ is capable of quenching the base of $O_2^{\bullet-}$ ($k_{O_2^{\bullet-}}$=9.8×10^8 $M^{-1}\cdot s^{-1}$). The reaction speed of TBA with $HO^{\bullet}$ is faster than $SO_4^{\bullet-}$ from 835 to 950 times ($k_{HO^{\bullet}}$=3.8-7.6×10^8 $M^{-1}\cdot s^{-1}$; $k_{SO_4^{\bullet-}}$=4.0-9.1×10^5 $M^{-1}\cdot s^{-1}$); therefore, TBA is capable of quenching $HO^{\bullet}$. Phenol can react at a high rate with both $SO_4^{\bullet-}$ and $HO^{\bullet}$ ($k_{SO_4^{\bullet-}}$=8.8×10^9 $M^{-1}\cdot s^{-1}$ and $k_{HO^{\bullet}}$=6.6×10^9 $M^{-1}\cdot s^{-1}$); thus phenol is capable of quenching both $SO_4^{\bullet-}$ and $HO^{\bullet}$.

The results in Fig. 14 show that the decrease in the decomposition efficiency of RhB when adding 1 mM of extinguishers is in the order of BQ (88.14%)>TBA (85.48%)>EDTA-2Na (47.17%)>PheOH (33.93%). Specifically, BQ and TBA did not significantly inhibit RhB degradation, while PheOH and EDTA-2Na strongly inhibited the reaction. Thus, the order of radicals that play a role in the decomposition of RhB is $SO_4^{\bullet-}$>h^+>$O_2^{\bullet-}$>$HO^{\bullet}$, in which $SO_4^{\bullet-}$ radicals and photo-excited holes h^+ play a major role in the decomposition of RhB. This also indicates that the ability to decompose RhB is due to the photocatalytic activity of the CNFe-97 material, not by the adsorption or thermal decomposition processes.

To evaluate the role of oxygen in the photocatalytic process, instead of continuously aerating, the air was replaced with nitrogen gas. Results show that when nitrogen was present, RhB degradation efficiency was reduced from 99.35% to 60.27%. Thus, oxygen molecules have a large role in the formation of $O_2^{\bullet-}$ and free radicals while it also reduces the electron-hole recombination. This is the reason that aeration is constantly required in practice for an effective photocatalytic reaction.

The photocatalytic mechanism of the semiconductor is closely related to the photocatalytic transition of the photoelectric electron-hole pair formed by light excitation. This is related to the covalent and conduction band energy values. Values of valence band energy (E_{VB}) and conductive band energy (E_{CB}) of materials are calculated by the following equations [35,36].

$$E_{VB}=X-E_e+0.5\times E_g \quad (3)$$

$$E_{CB}=E_{VB}-E_g \quad (4)$$

where X is the absolute electronegativity of the material. E_e is the energy of the free electrons on the hydrogen scale (about 4.50 V compared to the NHE) and E_g is the bandgap energy. In the literature, the X-value for pure g-C_3N_4 was reported at 4.73 eV [32,37]. Based on the UV-Vis DRS spectrum, the E_g value of g-C_3N_4 was

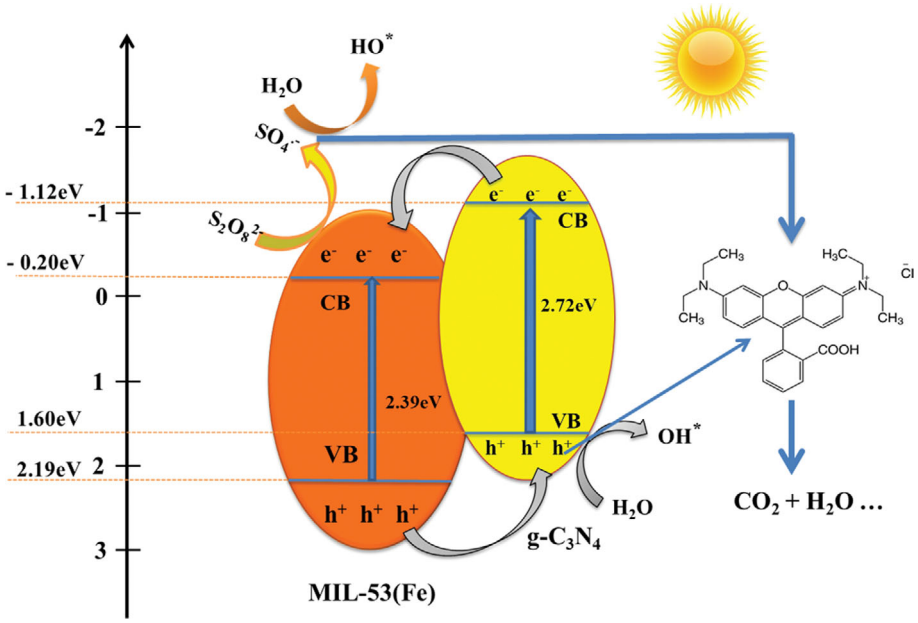

Fig. 15. Proposed mechanism of photocatalytic RhB treatment using CNFe-97.

determined to be 2.72 eV. Thus, the valence and conduction band energies of g-C_3N_4 were calculated to be 1.60 eV and −1.12 eV, respectively, corresponding to the bandgap energy of 2.72 eV. As a comparison, literature studies show that the valence and conduction band energies of MIL-53(Fe) were 2.19 eV and −0.2 eV, respectively, with a bandgap energy of 2.39 eV [13,33].

The photocatalytic mechanism is proposed in Fig. 15. After being activated by visible light, electrons in the CNFe-97 material are excited and jump onto the conduction band (CB), leaving the valence band (VB) as h^+ holes (Reaction 1). Since the conduction band energy of g-C_3N_4 (−1.12 eV) is lower than the conduction band energy of MIL-53(Fe) (−0.2 eV), the electrons move from the conduction band of g-C_3N_4 to MIL-53(Fe). In the valence region, the holes h^+ from MIL-53(Fe) transfer to g-C_3N_4. Reducing reactions then occur in the conduction region MIL-53(Fe), where the reaction between e^- and $S_2O_8^{2-}$, O_2 forms the free radicals of $SO_4^{\bullet-}$ and $O_2^{\bullet-}$ (Reactions 2 and 3). Sulfate radicals continue to react with water to form HO$^\bullet$ radicals (Reaction 4) while $O_2^{\bullet-}$ reacts with H^+ to form HO$^\bullet$ (Reaction 5). Oxidation reactions occur in the g-C_3N_4 valence region, where a reaction between the photo-excited hole h^+ and water forms the HO$^\bullet$ (Reaction 6). $SO_4^{\bullet-}$, h^+, $O_2^{\bullet-}$, and HO$^\bullet$ free radicals would decompose RhB directly into CO_2, H_2O, and other secondary pollutant products (Reaction 7). All of these processes occur continuously and significantly reduce the photo-excited electron-hole recombination in the CNFe-97 composite material.

$$\text{CNFe-97}+h\nu \rightarrow \text{CNFe-97}(e^- + h^+) \quad \text{(Re. 1)}$$

$$e^- + S_2O_8^{2-} \rightarrow SO_4^{\bullet-} + SO_4^{2-} \quad \text{(Re. 2)}$$

$$e^- + O_2 \rightarrow O_2^{\bullet-} \quad \text{(Re. 3)}$$

$$SO_4^{\bullet-} + H_2O \rightarrow SO_4^{2-} + HO^\bullet + H^+ \quad \text{(Re. 4)}$$

$$O_2^{\bullet-} + H^+ + 2e \rightarrow HO^\bullet + HO^- \quad \text{(Re. 5)}$$

$$h^+ + H_2O \rightarrow HO^\bullet + H^+ \quad \text{(Re. 6)}$$

$$[SO_4^{\bullet-}, h^+, O_2^{\bullet-}, \text{and } HO^\bullet] + \text{RhB} \rightarrow \text{Mineralized products} + CO_2 + H_2O + SO_4^{2-} \quad \text{(Re. 7)}$$

CONCLUSIONS

This study successfully synthesized g-C_3N_4/MIL-53(Fe) with an outstanding photocatalytic efficiency at 97 wt% MIL-53(Fe). MIL-53(Fe) was successfully modified with g-C_3N_4 to improve the photo-excited electron-hole separation, helping to speed up the decomposition of RhB. Besides the input concentration and catalytic content, the presence of oxidizing factors and pH conditions greatly affects the efficiency of RhB decomposition thanks to the enhancement of electron transport and Fe^{+2} formation, which is similar to the Fenton reaction. The mechanism of the reaction was also proposed, where free radicals have different roles in photocatalytic processes.

SUPPORTING INFORMATION

Additional information as noted in the text. This information is available via the Internet at http://www.springer.com/chemistry/journal/11814.

REFERENCES

1. M. Sabri, A. Habibi-Yangjeh and S. Vadivel, *Mater. Chem. Phys.*, **239**, 121988 (2020).
2. Y. Hong, H. Zhou, Z. Xiong, Y. Liu, G. Yao and B. Lai, *Chem. Eng. J.*, **391**, 123604 (2020).
3. M. Sabri, A. Habibi-Yangjeh, H. Chand and V. Krishnan, *Sep.*

Purif. Technol., **250**, 117268 (2020).
4. C. Bai, J. Bi, J. Wu, H. Meng, Y. Xu, Y. Han and X. Zhang, *Appl. Organomet. Chem.*, **32**, e4597 (2018).
5. W. Huang, N. Liu, X. Zhang, M. Wu and L. Tang, *Appl. Surf. Sci.*, **425**, 107 (2017).
6. L. Wang, X. Guo, Y. Chen, S. Ai and H. Ding, *Appl. Surf. Sci.*, **467-468**, 954 (2019).
7. L. Xie, Z. Yang, W. Xiong, Y. Zhou, J. Cao, Y. Peng, X. Li, C. Zhou, R. Xu and Y. Zhang, *Appl. Surf. Sci.*, **465**, 103 (2019).
8. C.-C. Wang, X.-H. Yi and P. Wang, *Appl. Catal., B*, **247**, 24 (2019).
9. J. Wen, J. Xie, X. Chen and X. Li, *Appl. Surf. Sci.*, **391**, 72 (2017).
10. L. Tang, Z.-q. Lv, Y.-c. Xue, L. Xu, W.-h. Qiu, C.-m. Zheng, W.-q. Chen and M.-h. Wu, *Chem. Eng. J.*, **374**, 975 (2019).
11. F. A. Sofi and K. Majid, *Mater. Chem. Front.*, **2**, 942 (2018).
12. J. Hong, C. Chen, F. E. Bedoya, G. H. Kelsall, D. O'Hare and C. Petit, *Catal. Sci. Technol.*, **6**, 5042 (2016).
13. M. Salimi, A. Esrafili, A. J. Jafari, M. Gholami and H. R. Sobhi, *Inorg. Chem. Commun.*, **111**, 107565 (2020).
14. D. Guo, R. Wen, M. Liu, H. Guo, J. Chen and W. Weng, *Appl. Organomet. Chem.*, **29**, 690 (2015).
15. L. Ai, C. Zhang, L. Li and J. Jiang, *Appl. Catal., B*, **148-149**, 191 (2014).
16. S. Kumar, T. Surendar, B. Kumar, A. Baruah and V. Shanker, *RSC Adv.*, **4**, 8132 (2014).
17. S. P. Manalu, T. S. Natarajan, M. De Guzman, Y.-F. Wang, T.-C. Chang, F.-C. Yen and S.-J. You, *Green Processing and Synthesis*, **7**, 493 (2018).
18. R. Nivetha, P. Kollu, K. Chandar, S. Pitchaimuthu, S. K. Jeong and A. N. Grace, *RSC Adv.*, **9**, 3215 (2019).
19. T. A. Vu, G. H. Le, C. D. Dao, L. Q. Dang, K. T. Nguyen, Q. K. Nguyen, P. T. Dang, H. T. K. Tran, Q. T. Duong, T. V. Nguyen and G. D. Lee, *RSC Adv.*, **5**, 5261 (2015).
20. W. Huang, N. Liu, X. Zhang, M. Wu and L. Tang, *Appl. Surf. Sci.*, **425**, 107 (2017).
21. M. Al Haydar, H. R. Abid, B. Sunderland and S. Wang, *Drug Des. Devel. Ther.*, **11**, 2685 (2017).
22. P. George, K. Chaudhari and P. Chowdhury, *J. Mater. Sci.*, **53**, 11694 (2018).
23. P. G. Yot, Z. Boudene, J. Macia, D. Granier, L. Vanduyfhuys, T. Verstraelen, V. van Speybroeck, T. Devic, C. Serre, G. Férey, N. Stock and G. Maurin, *Chem. Commun.*, **50**, 9462 (2014).
24. V. Shanmugam, A. L. Muppudathi, S. Jayavel and K. S. Jeyaperumal, *Arabian J. Chem.*, **13**, 2439 (2018).
25. W. Xiong, G. Zeng, Z. Yang, Y. Zhou, C. Zhang, M. Cheng, Y. Liu, L. Hu, J. Wan, C. Zhou, R. Xu and X. Li, *Sci. Total Environ.*, **627**, 235 (2018).
26. C. Bai, J. Bi, J. Wu, H. Meng, Y. Xu, Y. Han and X. Zhang, *Appl. Organomet. Chem.*, **32**, e4597 (2018).
27. Y. Zhang, J. Liu, G. Wu and W. Chen, *Nanoscale*, **4**, 5300 (2012).
28. T.-F. Yeh, C.-Y. Teng, S.-J. Chen and H. Teng, *Adv. Mater.*, **26**, 3297 (2014).
29. C. Zhang, L. Ai and J. Jiang, *J. Mater. Chem. A*, **3**, 3074 (2015).
30. X. Feng, H. Chen and F. Jiang, *J. Colloid Interface Sci.*, **494**, 32 (2017).
31. R. Liang, F. Jing, L. Shen, N. Qin and L. Wu, *J. Hazard. Mater.*, **287**, 364 (2015).
32. Y. Gong, B. Yang, H. Zhang and X. Zhao, *J. Mater. Chem. A*, **6**, 23703 (2018).
33. S. Miao, Z. Zha, Y. Li, X. Geng, J. Yang, J. Yang and S. Cui, *J. Photochem. Photobiol. A*, **380**, 111862 (2019).
34. Z. Huang, X. Zeng, K. Li, S. Gao, Q. Wang and J. Lu, *ACS Appl. Mater. Interfaces*, **9**, 41120 (2017).
35. B. Zhang, H. Shi, Y. Yan, C. Liu, X. Hu, E. Liu and J. Fan, *Colloids Surf. Physicochem. Eng. Aspects*, **608**, 125598 (2021).
36. W. Wang, T. An, G. Li, D. Xia, H. Zhao, J. C. Yu and P. K. Wong, *Appl. Catal., B*, **217**, 570 (2017).
37. H. Heidarpour, M. Padervand, M. Soltanieh and M. Vossoughi, *Chem. Eng. Res. Des.*, **153**, 709 (2020).